


Data-Driven Retrospective Correction of B_1 Field Inhomogeneity in Fast Macromolecular Proton Fraction and R_1 Mapping

Vasily L. Yarnykh 

Abstract—Correction of B_1 field non-uniformity is critical for many quantitative MRI methods including variable flip angle (VFA) T_1 mapping and single-point macromolecular proton fraction (MPF) mapping. The latter method showed promising results as a fast and robust quantitative myelin imaging approach and involves VFA-based $R_1 = 1/T_1$ map reconstruction as an intermediate processing step. The need for B_1 correction restricts applications of the above methods, since B_1 mapping sequences increase the examination time and are not commonly available in clinics. A new algorithm was developed to enable retrospective data-driven simultaneous B_1 correction in VFA R_1 and single-point MPF mapping. The principle of the algorithm is based on different mathematical dependences of B_1 -related errors in R_1 and MPF allowing extraction of a surrogate B_1 field map from uncorrected R_1 and MPF maps. To validate the method, whole-brain R_1 and MPF maps with isotropic 1.25 mm³ resolution were obtained on a 3 T MRI scanner from 11 volunteers. Mean parameter values in segmented brain tissues were compared between three reconstruction options including the absence of correction, actual B_1 correction, and surrogate B_1 correction. Surrogate B_1 maps closely reproduced actual patterns of B_1 inhomogeneity. Without correction, B_1 non-uniformity caused highly significant biases in R_1 and MPF ($P < 0.001$). Surrogate B_1 field correction reduced the biases in both R_1 and MPF to a non-significant level ($0.1 \leq P \leq 0.8$). The described algorithm obviates the use of dedicated B_1 mapping sequences in fast single-point MPF mapping and provides an alternative solution for correction of B_1 non-uniformities in VFA R_1 mapping.

Index Terms— B_1 field, macromolecular proton fraction (MPF), magnetization transfer, myelin, quantitative MRI, T_1 relaxation.

Manuscript received March 8, 2021; accepted June 6, 2021. Date of publication June 10, 2021; date of current version November 30, 2021. This work was supported in part by the National Institutes of Health through the High Impact Neuroscience Research Resource under Grant R24 NS104098, Grant R21 NS109727, and Grant R01 EB027087 (algorithm and software development, image processing); in part by the National Multiple Sclerosis Society under Grant RG 4864A1/1 (source MRI data); and in part by the Russian Science Foundation under Grant 19-75-20142 (source MRI data).

This work involved human subjects in its research. Approval of all ethical and experimental procedures and protocols was granted by the University of Washington under Application No. 44547.

The author is with the Department of Radiology, University of Washington, Seattle, WA 98109 USA, and also with the Research Institute of Biology and Biophysics, Tomsk State University, 634050 Tomsk, Russia (e-mail: yarnykh@uw.edu).

This article has supplementary downloadable material available at <https://doi.org/10.1109/TMI.2021.3088258>, provided by the authors.

Digital Object Identifier 10.1109/TMI.2021.3088258

I. INTRODUCTION

NON-UNIFORMITY of transmitter radiofrequency (RF) magnetic field (B_1) is commonly acknowledged as a major source of errors in various quantitative MRI methods [1]. B_1 inhomogeneity is dramatically amplified with an increase in magnetic field strength, thus rendering mandatory B_1 field mapping for error correction in certain high-field quantitative imaging applications [1]. One of such applications is the variable flip angle (VFA) T_1 mapping method [2]–[4], which gained broad popularity due to its acquisition speed and the capability to generate high-resolution 3D parametric maps with a clinically acceptable scan time. In the most time-efficient design [3], the VFA method utilizes two spoiled gradient-echo (GRE) images with T_1 and proton density (PD) contrast weightings to compute T_1 and PD parametric maps. However, this technique is extremely sensitive to B_1 errors that may cause up to several hundred percent bias in T_1 estimates obtained using 3 T MRI equipment [4]. Another quantitative MRI method that heavily relies on B_1 correction is single-point macromolecular fraction (MPF) mapping [5], [6], which attracted significant interest over the past years as a fast and robust technique for quantitative imaging of myelin in the brain [7]–[16]. Particularly, MPF demonstrated strong correlations with histologically measured myelin density in animal models [7]–[10] and showed promise as a biomarker of myelin in human studies of multiple sclerosis [11], [12], mild traumatic brain injury [13], and brain development [14]–[16]. The single-point method in its recent synthetic-reference modification [6] reconstructs an MPF map from a single spoiled GRE image with magnetization transfer (MT) contrast and T_1 and PD maps obtained by the two-point VFA technique, thus utilizing only three source images (T_1 -, PD-, and MT-weighted) as input data. Although to a lesser degree than T_1 , MPF estimates obtained by this method are also subjected to B_1 -related errors, which may approach 30-40% in the relative scale for a typical range of B_1 non-uniformities occurring at 3 T [17]. The need for B_1 correction substantially restricts clinical applications of both VFA T_1 and MPF mapping techniques due to examination time penalties associated with a supplementary B_1 mapping scan and limited availability of specialized B_1 mapping sequences on clinical MRI systems.

As substantiated by the detailed analysis provided below, propagation of B_1 errors into MPF and longitudinal relaxation rate $R_1 = 1/T_1$ is described by principally different math-

emathical relations. This study aimed to exploit distinctions between the mathematical descriptions of B_1 -related errors in R_1 and MPF in order to develop a data-driven algorithm for simultaneous retrospective correction of B_1 inhomogeneity in corresponding parametric maps without additional B_1 field mapping sequences.

II. THEORY

A. Theory of Errors in MPF Due to B_1 Inhomogeneity

As a starting point, we use the matrix formulation of a signal equation derived for a spoiled gradient-echo sequence with MT preparative pulse (MT-GRE) based on the two-pool pulsed MT theory [18], [19]. This model considers periodic pulsed saturation applied to the two-pool model with cross-relaxation, where tissue is presented as a system containing free water protons (free pool, identified below by superscript index ‘‘F’’) and macromolecular protons (bound pool, identified below by superscript index ‘‘B’’). Evolution of magnetization is analyzed separately during four time intervals comprising the sequence cycle: off-resonance saturation pulse (t_m), delay for spoiling gradient (t_s), readout pulse (t_p), and delay for signal readout and relaxation (t_r). Assuming that the pulsed steady state is established, the resulting equation for the longitudinal magnetization can be written in matrix form as

$$\mathbf{M}_z = (\mathbf{I} - \mathbf{E}_s \mathbf{E}_m \mathbf{E}_r \mathbf{C})^{-1} \{ [\mathbf{E}_s \mathbf{E}_m (\mathbf{I} - \mathbf{E}_r) + (\mathbf{I} - \mathbf{E}_s)] \mathbf{M}_{\text{eq}} + \mathbf{E}_s (\mathbf{I} - \mathbf{E}_m) \mathbf{M}_{\text{ss}} \}, \quad (1)$$

where \mathbf{M}_{eq} is the vector of equilibrium magnetization with elements $M_0(1-f)$ and M_0f , where f is MPF; \mathbf{M}_{ss} is the vector of steady-state longitudinal magnetization with explicit notation given elsewhere [19]; \mathbf{M}_z is the vector with components M_z^F and M_z^B corresponding to the longitudinal magnetization immediately before the excitation pulse; \mathbf{I} is the unit matrix; the matrix term $\mathbf{E}_m = \exp((\mathbf{R} + \mathbf{W})t_m)$ describes off-resonance saturation by an RF pulse with duration t_m ; the terms $\mathbf{E}_s = \exp(\mathbf{R}t_s)$ and $\mathbf{E}_r = \exp(\mathbf{R}t_r)$ describe relaxation during delays before (t_s) and after (t_r) an excitation RF pulse; and the diagonal matrix \mathbf{C} corresponds to instant rotation of the magnetization M_z^F by an excitation pulse. The relaxation matrix \mathbf{R} is defined as:

$$\mathbf{R} = \begin{bmatrix} -R_1^F - Rf/(1-f) & R \\ Rf/(1-f) & -R_1^B - R \end{bmatrix}, \quad (2)$$

where R_1^F and R_1^B are the longitudinal relaxation rates of the pools, and R is the exchange rate constant for MT from the bound to the free pool.

B_1 non-uniformity can be described by the scaling factor c defined as the ratio of actual to nominal B_1 field in a voxel:

$$c = B_{1a}/B_{1\text{nom}}. \quad (3)$$

In the presence of B_1 inhomogeneity, the matrix \mathbf{C} describing the effect of the excitation pulse with the nominal flip angle α is expressed as

$$\mathbf{C} = \text{diag}(\cos(c\alpha), 1). \quad (4)$$

The saturation matrix \mathbf{W} is scaled with the squared c :

$$\mathbf{W} = -c^2 \text{diag}(W^F, W^B), \quad (5)$$

where $W^{F,B}$ are the saturation rates for the pools averaged over the saturation pulse duration, which are expressed as

$$W^{F,B} = \pi \omega_{1\text{rms}}^2 g^{F,B}(\Delta, T_2^{F,B}), \quad (6)$$

where $g^{F,B}(\Delta, T_2^{F,B})$ are the spectral line shapes of the pools dependent on their T_2 and offset frequency Δ , and $\omega_{1\text{rms}}$ is the root-mean-square nominal saturation power:

$$\omega_{1\text{rms}} = \frac{\text{FAMT}}{t_m} \frac{\pi}{180} \frac{\left(\int_0^{t_m} b_1^2(t) dt \right)^{1/2}}{\int_0^{t_m} b_1(t) dt}, \quad (7)$$

which is calculated from the flip angle (FAMT), duration (t_m), and envelope function ($b_1(t)$) of the saturation pulse [5]. The line shapes $g^{F,B}(\Delta, T_2^{F,B})$ are commonly approximated by the Lorentzian and SuperLorentzian functions for the free and bound pool, respectively [18], [20]. Note that according to equations (4) – (7), all RF-related variables are defined by the nominal values calculated from the pulse sequence parameters, while their spatial dependence on B_1 field is solely described by the scaling factor c .

Applying the first-order approximation to the exponential terms and using the identity $\mathbf{R}\mathbf{M}_{\text{eq}} = (\mathbf{R} + \mathbf{W})\mathbf{M}_{\text{ss}}$, (1) can be rewritten as:

$$\mathbf{M}_z \approx (\mathbf{R} + \tau \mathbf{W} + \text{TR}^{-1} \ln \mathbf{C})^{-1} \mathbf{R}\mathbf{M}_{\text{eq}}, \quad (8)$$

where $\tau = t_m/\text{TR}$ is the duty cycle of the saturation pulse. If the sequence is completely spoiled, the equation for the MT-weighted signal can be obtained from (8):

$$S_{\text{mt}} = AM_z^F \sin(c\alpha) \exp(-\text{TE}/T_2^*), \quad (9)$$

where A is the coil reception profile and M_z^F is given by

$$\begin{aligned} M_z^F &\approx \frac{M_0(1-f)(R_1^F R_1^B + R_1^F R + R_1^B R f(1-f)^{-1} + R_1^F c^2 \tau W^B)}{R_1^F R_1^B + R_1^F R + R_1^B R f(1-f)^{-1} \\ &\quad + (R_1^F + R f(1-f)^{-1}) c^2 \tau W^B \\ &\quad + (R_1^B + R + c^2 \tau W^B)(c^2 \tau W^F - \text{TR}^{-1} \ln \cos(c\alpha))} \end{aligned} \quad (10)$$

To obtain explicit equation describing the relationship between the measured MPF and B_1 non-uniformity, we further assume that the relaxation rates of the pools are equal to the observed R_1 , $R_1^F = R_1^B = R_1$ that is the standard assumption in the single-point MPF mapping method [5], [6]. After rearrangements, an approximated first-order equation for the observed MT-weighted signal can be expressed as

$$\begin{aligned} S_{\text{mt}} &\approx \text{PDR}_1 \sin(c\alpha) \{ R_1 - \text{TR}^{-1} \ln \cos(c\alpha) + c^2 \tau W^F \\ &\quad + \frac{fR(\text{TR}^{-1} \ln \cos(c\alpha) + c^2 \tau W^B - c^2 \tau W^F)}{R + (1-f)(R_1 + c^2 \tau W^B)} \}^{-1}, \end{aligned} \quad (11)$$

where the effective proton density (PD) absorbs the factors of the coil reception profile A , actual proton density $M_0(1-f)$, and T_2^* decay:

$$\text{PD} = AM_0(1-f) \exp(-\text{TE}/T_2^*). \quad (12)$$

The PD value is identical for all three scans (MT-, PD, and T_1 -weighted) acquired in the single-point synthetic reference MPF mapping method [6].

Computation of MPF in the single-point synthetic reference method with unknown B_1 non-uniformity can be approximated as the single-parameter fit of the signal model S_{mt}^m calculated with the nominal values of RF-related variables ($c = 1$) and measured by the VFA method values of PD and R_1 containing B_1 -related errors (PD_m and R_{1m} , respectively) to the experimental signal S_{mt} given by (11):

$$f_m = \arg \min [S_{mt}(f, PD, R_1, c) - S_{mt}^m(f_m, PD_m, R_{1m}, c = 1)]^2, \quad (13)$$

where f_m is the experimentally measured MPF value containing an error caused by B_1 non-uniformity. To incorporate the effect of B_1 non-uniformity on PD and R_1 measurements, we adopt the earlier results by Helms *et al.* [4] for the corresponding errors in the two-point VFA method based on a small flip angle approximation:

$$PD_m = cPD \quad (14)$$

and

$$R_{1m} = c^{-2} R_1. \quad (15)$$

With (14) and (15), the equation for S_{mt}^m takes the form:

$$S_{mt}^m \approx cPDR_1 \sin \alpha \{ R_1 - c^2 TR^{-1} \ln \cos \alpha + c^2 \tau W^F + \frac{c^2 f_m R (TR^{-1} \ln \cos \alpha + \tau W^B - \tau W^F)}{R + (1 - f_m)(c^{-2} R_1 + \tau W^B)} \}^{-1}. \quad (16)$$

It should be pointed out that the expression for S_{mt}^m (16) now explicitly depends on c as a result of substitution of (14) and (15) for PD_m and R_{1m} . Equation (13) can be exactly solved with respect to f_m by equating the analytical signal expressions $S_{mt}^m = S_{mt}$ given by (11) and (16). For a small flip angle α , the solution can be greatly simplified by applying the approximations $c \sin \alpha \approx \sin(c\alpha)$ and $c^2 \ln \cos \alpha \approx \ln \cos(c\alpha)$, which follow from the Maclaurin series expansion. Under the above approximations,

$$f_m \approx f \frac{c^2(\tau W^B + R) + R_1}{c^2(c^2 \tau W^B + R + R_1) + f(1 - c^2)(c^2 \tau W^B + R)}. \quad (17)$$

Equation (17) can be further simplified assuming that $R_1 \ll R$. This assumption is supported by the experimental data suggesting that R is about 20-40-fold larger than R_1 for most tissues [21]. Additionally, the second term in the denominator of (17) is much smaller than the first term and can be neglected. Accordingly, (17) is reduced to

$$f_m \approx f \frac{\tau W^B + R}{c^2 \tau W^B + R}. \quad (18)$$

Analysis of formulas (17) and (18) results in several important conclusions:

- 1) The main source of B_1 -related errors in single-point MPF mapping [5], [6] is the propagation of B_1 non-uniformity into the spatial variations of the saturation rate W^B .

- 2) According to (18), the relative error in MPF is almost independent of tissue properties in the brain, since the parameters R and T_2^B are nearly identical for brain tissues and kept constant in the single-point algorithm [5]. The residual tissue dependence associated with the small terms including R_1 and f in (17) is negligible due to the dominant effect of W^B .
- 3) The errors caused by the effect of B_1 non-uniformity on the excitation flip angle and direct saturation of the free pool (W^F) are negligibly small, since the corresponding terms are eliminated during the derivation of (17).

B. Estimation of B_1 Inhomogeneity From the Mismatch Between MPF and R_1 Measurement Errors

The key idea of the proposed data-driven algorithm is the derivation of the B_1 field non-uniformity factor c from the measured R_1 and MPF values based on the fact that B_1 -related errors in these parameters have different functional forms given by (15) and (17). To apply this approach, one needs to find a function defining a relationship between R_1 and MPF in the absence of B_1 errors. For this purpose, we adopt a general linear relaxometry model [22], which describes the longitudinal relaxation rate in brain tissues as a weighted sum of macromolecular and paramagnetic contributions:

$$R_1 = R_{1w} + r_m[M] + \sum_i r_{pi}[P]_i, \quad (19)$$

where R_{1w} is the longitudinal relaxation rate of pure water, r_m and $[M]$ are the relaxivity and molar concentration of the macromolecular protons modulating R_1 via cross-relaxation and chemical exchange, and r_{pi} and $[P]_i$ are the relaxivities and molar concentrations of paramagnetic ions (primarily iron). Equation (19) can be rewritten with inclusion of MPF:

$$R_1 = R_{1w} + r_m[W] \frac{f}{1-f} + \frac{1}{V(1-f)} \sum_i r_{pi} n_i, \quad (20)$$

where $[W]$ is the molar concentration of water protons, V is the tissue volume, and n_i are the molar amounts of paramagnetic substances. Note that the concentration of macromolecular protons in (20) is expressed from the definition of MPF, $f = [M]/([M] + [W])$, and concentrations $[P]_i$ are defined as the molar amounts n_i per water volume in tissue, which can be approximated as $V(1-f)$. After rearrangements, (20) can be presented as a linear function in coordinates R_1 and $f/(1-f)$:

$$R_1 = r_0 + r_f f/(1-f), \quad (21)$$

where the coefficients r_0 and r_f absorb all unrelated to MPF contributions. We further assume that the constants r_0 and r_f for the brain can be determined as population-average values from experimental B_1 -corrected measurements, and their tissue-dependent variability is negligible for the purpose of B_1 field estimation. The validity of these assumptions is investigated later.

Measured R_{1m} and f_m values in the presence of B_1 errors can be substituted into (21) after transforming into the actual values according to the error models given by (15) and (17).

For MPF, the explicit recalculation formula is obtained from (17) by solving for f :

$$f \approx f_m \frac{c^2 + R(\tau W^B + R_{1m})^{-1}}{1 + R(\tau W^B + R_{1m})^{-1} - f_m(1 - c^2)}. \quad (22)$$

After substitution of (15) and (22) into (21), the resulting equation can be solved relative to the B_1 field scaling factor c . To emphasize the distinction between the approximated and actual B_1 estimates, we further denote this solution as surrogate B_1 field (B_{1s}) with the scaling factor c_s , which should be treated as an approximation of the actual field B_{1a} :

$$c \approx c_s = \sqrt{\frac{r_0(1 - f_m) + r_f P f_m}{R_{1m}(1 - f_m) - r_f(1 - P)f_m}}, \quad (23)$$

where $P = R/(R + \tau W^B + R_{1m})$. As such, a surrogate B_{1s} field map can be reconstructed according to (23) from uncorrected R_1 and MPF maps under the assumption of constant regression coefficients r_0 and r_f across the tissues of interest and further used to compute corrected R_1 and MPF maps, similar to an actual B_{1a} map.

C. Reparameterization of the Direct Saturation Effect

In the single-point MPF mapping algorithm [5], the two-pool model parameters with small tissue-dependent variations are constrained by using the experimentally determined standard whole brain values. Particularly, constant values of $R = 19 \text{ s}^{-1}$, $T_2^B = 10 \text{ } \mu\text{s}$, and the product of the observed R_1 and T_2 of the free pool, $R_{1m}T_2^F = 0.022$, were used for MPF mapping at 3 T [5]. The latter quantity is field-dependent [5], [23], [24] and needs to be specified for a particular field strength. The product $R_{1m}T_2^F$ is used to estimate T_2^F , which determines the saturation rate of the free pool W^F (6). If off-resonance saturation is applied at relatively high offset frequencies (4-7 kHz) as suggested for the optimal fast MPF mapping protocol design [5], the effect of W^F is negligibly small. However, careful consideration of direct saturation is required for applications of the proposed method with clinical MT-weighted sequences, where offset frequencies are typically in a range 1-1.5 kHz [14]. If measured in the presence of large B_1 non-uniformity, R_{1m} may artificially inflate the errors associated with the direct saturation term. As a more robust approach to correct for the direct saturation effect, we propose an estimate based on the global correlation given by (21), such that the constraint for T_2^F takes the form

$$T_2^F = 0.022(1 - f_m)(r_0(1 - f_m) + r_f f_m)^{-1} \quad (24)$$

for 3 T magnetic field. The main advantage of this parameterization is that an estimate of T_2^F and, therefore, calculated W^F , becomes much less dependent on B_1 inhomogeneity. More detailed comparison between both parameterization approaches is given in the Results section.

III. METHODS

A. Simulations

To investigate R_1 and MPF measurement errors caused by B_1 inhomogeneity and the effect of their correction by

the proposed algorithm, PD-, T_1 -, and MT-weighted signal intensities were simulated using the matrix two-pool pulsed steady-state model (1)-(7) for a series of B_1 field scaling factors c . Then R_1 , PD, and MPF values were computed using the single-point synthetic reference algorithm [6] at the nominal flip angles of RF pulses in all sequences. The resulting R_1 and MPF estimates (R_{1m} and f_m) containing B_1 -related errors were used to compute the surrogate B_1 field scaling factor c_s according to (23). To simulate the effect of surrogate B_1 field correction, R_1 , PD, and MPF values were refitted using the same procedure after scaling all flip angles by the factor c_s . The models with both the previous ($R_{1m}T_2^F = 0.022$) and new (24) parameterization of the direct saturation effect were tested. Additionally, to assess the validity of approximations applied in the algorithm, R_{1m} and f_m values were generated using the analytical expressions (15) and (17).

Simulations were carried out for the two sets of the two-pool model parameters corresponding to the average values in the brain white matter (WM) and gray matter (GM). The following parameters were used: MPF = 12.5%, $R_1 = 0.95 \text{ s}^{-1}$, $R = 19 \text{ s}^{-1}$, $T_2^F = 23 \text{ ms}$, and $T_2^B = 10 \text{ } \mu\text{s}$ for WM and MPF = 6.5%, $R_1 = 0.63 \text{ s}^{-1}$, $R = 19 \text{ s}^{-1}$, $T_2^F = 35 \text{ ms}$, and $T_2^B = 10 \text{ } \mu\text{s}$ for GM. Pulse sequence parameters were the same as those detailed in the experimental protocols outlined below. The coefficients r_0 and r_f were set according to their experimentally measured values as detailed below. The effect of uncertainties in the constants r_0 and r_f was assessed by varying their values in a range of two standard deviations (SD) of their experimental measurements. Simulations were performed using custom-written C-language software.

B. Study Participants

The study was approved by the Institutional Review Board and all participants provided written informed consent. 3D R_1 and MPF maps were obtained from 11 healthy volunteers (7 females; mean age \pm SD = 44.8 \pm 13.8 years; age range 26-65 years) using an optimized high-resolution protocol [6], [17] on a research MRI scanner. Additionally, one participant (male, 53-year-old) was scanned with a lower-resolution protocol on a clinical MRI unit using standard manufacturer's sequences.

C. MRI Acquisition

Images from 11 participants were acquired on a 3 T research MRI scanner (Achieva; Philips Medical Systems, Best, Netherlands) with an eight-channel head coil and modified software for optimal performance of imaging sequences. Software modifications included optimal settings of the saturation pulse [5] in the MT-weighted sequence and optimal RF and gradient spoiling [25]. The 3D MPF mapping protocol was implemented according to the single-point synthetic reference method [6] and included the PD-weighted (TR = 21 ms, $\alpha = 4^\circ$, scan time 4 min 21 s), T_1 -weighted (TR = 21 ms, $\alpha = 25^\circ$, scan time 4 min 21 s), and MT-weighted (TR = 28 ms, $\alpha = 10^\circ$, scan time 5 min 48 s) imaging sequences. Off-resonance saturation in the MT-weighted sequence was

achieved by the single-lobe-sinc pulse with Gaussian apodization, $\Delta = 4$ kHz, $\text{FA}_{\text{MT}} = 560^\circ$, and $t_m = 12$ ms. These settings resulted in $\omega_{1\text{rms}} = 940$ rad/s, $\tau = 0.42$, and $W^{\text{B}} = 18.1$ s $^{-1}$. All images were acquired in the sagittal plane with dual-echo readout ($\text{TE}_1/\text{TE}_2 = 2.3$ ms/6.9 ms), $\text{FOV} = 240 \times 240 \times 180$ mm 3 , and actual voxel size of $1.25 \times 1.25 \times 1.25$ mm 3 interpolated to $0.63 \times 0.63 \times 0.63$ mm 3 after zero-padded Fourier transform. Actual flip-angle imaging (AFI) B_1 maps [26] were obtained with $\text{TR}_1/\text{TR}_2/\text{TE} = 40/160/2.3$ ms, $\alpha = 60^\circ$, scan time of 3 min 26 s, and voxel size of $2.5 \times 2.75 \times 5.0$ mm 3 interpolated to $0.63 \times 0.63 \times 0.63$ mm 3 . Parallel imaging (SENSE) [27] was used for all scans in two phase encoding directions with acceleration factors 1.5 and 1.2.

A prototype clinical protocol was tested on a single study participant. Data were obtained using a 3 T clinical scanner (Ingenia; Philips Medical Systems, Best, Netherlands) with a 16-channel head coil. The fast MPF mapping technique was built on unmodified manufacturer's sequences. The PD-weighted ($\text{TR} = 20$ ms, $\alpha = 3^\circ$, scan time 2 min 38 s), T_1 -weighted ($\text{TR} = 20$ ms, $\alpha = 20^\circ$, scan time 2 min 38 s), and MT-weighted ($\text{TR} = 70$ ms, $\alpha = 10^\circ$, scan time 9 min 12 s) images were acquired. The preset manufacturer's three-lobe-sinc pulse with Gaussian apodization, $\Delta = 1.1$ kHz, $\text{FA}_{\text{MT}} = 520^\circ$, and $t_m = 34$ ms was used for off-resonance saturation. These parameters corresponded to $\omega_{1\text{rms}} = 612$ rad/s, $\tau = 0.49$, and $W^{\text{B}} = 14.9$ s $^{-1}$. Images were acquired in the axial plane with $\text{TE} = 2.3$ ms, $\text{FOV} = 240 \times 200 \times 240$ mm 3 , and actual voxel size of $1.25 \times 1.5 \times 4.0$ mm 3 interpolated to $1.0 \times 1.0 \times 2.0$ mm 3 after zero-padded Fourier transform. Additionally, an AFI B_1 map (scan time 4 min 22 s) was obtained with the sequence parameters same as above and voxel size of $2.5 \times 2.75 \times 5.0$ mm 3 interpolated to $1.0 \times 1.0 \times 2.0$ mm 3 .

D. Image Processing and Analysis

Eleven datasets obtained with the optimal high-resolution protocol were processed to determine the mean algorithm constants r_0 and r_f and compare B_1 field correction options including the absence of correction, correction with an actual B_1 map ($B_{1\text{a}}$), and surrogate B_1 field ($B_{1\text{s}}$) correction. A single dataset acquired using the prototype clinical protocol was processed with the above B_1 correction options to demonstrate the compatibility of the proposed algorithm with unmodified manufacturer's MRI sequences.

Prior to map reconstruction, individual echo images in the high-resolution datasets were averaged to increase SNR [28]. Extracranial tissues were removed from source images by applying a brain mask created from the PD-weighted image using the brain extraction tool [29] available in FSL software (FMRIB Software Library; <http://www.fmrib.ox.ac.uk/fsl>). R_1 maps were computed using the analytical solution for the two-point VFA method [3]. MPF maps were reconstructed using the single-point synthetic reference algorithm [6] with T_2^{F} calculated according to (24) and the fixed values of $R = 19$ s $^{-1}$ and $T_2^{\text{B}} = 10$ μs . MPF fit was performed for the voxels with the non-zero saturation effect defined as

$(S_{\text{ref}} - S_{\text{mt}})/S_{\text{ref}} > 0.01$, where S_{ref} is the synthetic reference image intensity calculated from uncorrected PD_m and R_{1m} maps. Surrogate $B_{1\text{s}}$ maps were calculated from uncorrected R_{1m} and MPF (f_m) maps according to (23) with the same coefficients r_0 and r_f for all datasets. Their values were determined from the regression analysis of R_1 and MPF measurements in segmented brain tissues as detailed below. Noise and residual tissue-dependent variations in both actual and surrogate B_1 maps were minimized by applying a 3D trimmed mean filter with 12-voxel radius and field non-uniformity thresholds $0.3 < c < 2.0$. All reconstruction procedures were carried out using custom-written C-language software.

High-resolution MPF maps reconstructed with actual B_1 correction were segmented into three tissue classes (WM, GM, and a mixed class containing voxels with partial volume of cerebrospinal fluid (PVCFSF)) similar to the procedure described earlier [6], [17]. Segmentation was performed using the automated tool FAST [30] in FSL software with the Markov random field weighting parameter 0.25 and tissue-specific priors of 12% for WM, 6% for GM, and 1% for PVCFSF. Examples of segmented tissue masks for similar datasets can be found elsewhere [6], [17]. Mean R_1 and MPF values calculated within each tissue mask for each reconstruction option were used in subsequent analyses.

To examine agreement between actual and surrogate B_1 corrections on the voxel level, voxel-based Bland-Altman plots were constructed for each individual dataset from the B_1 scaling factor (c or c_s) maps and corrected R_1 and MPF maps. The voxel-based Bland-Altman plots were computed as two-dimensional histograms of the mean value and difference for each pair of voxel intensities with the bin sizes of 0.004, 0.02%, and 0.004 s $^{-1}$ for B_1 , R_1 , and MPF, respectively. Additionally, relative error maps for B_1 , R_1 , and MPF were reconstructed as the difference between actual and surrogate B_1 corrections divided by the actual map.

E. Statistical Analysis

The coefficients r_0 and r_f were determined from linear regression of R_1 on $\text{MPF}/(1-\text{MPF})$ values in segmented brain tissues measured from the datasets reconstructed with actual B_1 correction. The effect of B_1 field corrections on R_1 and MPF in each tissue class was examined using repeated-measures ANOVA with three levels of the within-subject factor (no correction, actual B_1 correction, and surrogate B_1 correction). Greenhouse-Geisser correction for non-sphericity was applied to the degrees of freedom. Significance of the biases between B_1 correction options was assessed using post-hoc Tukey honest significant difference tests. Bland-Altman plots were used to investigate an agreement between corrected and uncorrected R_1 and MPF values across the brain tissues. The limits of agreement were calculated as the mean difference $\pm 1.96\text{SD}$ of the mean difference. Agreement between different reconstructions was also characterized by the within-subject coefficient of variation (CoV). Two-tailed tests were used with the significance level of $P < 0.05$. Statistical analysis was carried out in Statistica (StatSoft Inc, Tulsa, OK, USA) software.

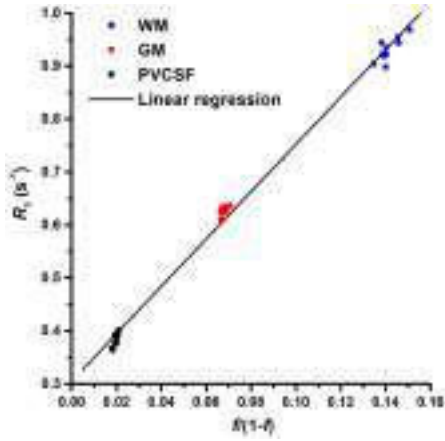


Fig. 1. Linear regression of R_1 on $\text{MPF}/(1-\text{MPF})$ measurements in segmented brain tissues based on 11 high-resolution datasets reconstructed with actual B_1 correction. Black, red, and blue points correspond to the PVCSF, GM, and WM tissue classes, respectively.

IV. RESULTS

A. Estimation of the Algorithm Constants

Linear regression across the mean parameter measurements based on B_{1a} -corrected maps in the brain tissues (WM, GM, and PVCSF) for all subjects (Fig. 1) showed strong linear relationship between R_1 and the MPF-derived quantity $f/(1-f)$, which was described by the empirical equation $R_1 = 0.31 + 4.47f/(1-f)$ ($r = 0.998$, $P < 0.001$). Regression analysis of individual datasets resulted in the following mean values \pm SD of the regression coefficients: $r_0 = 0.31 \pm 0.01$ (range 0.29-0.32) and $r_f = 4.47 \pm 0.13$ (range 4.29-4.76). Based on these results, the rounded values of the constants $r_0 = 0.3$ and $r_f = 4.5$ were uniformly used in subsequent reconstruction of surrogate B_1 field maps and simulations.

B. Simulations

Simulated dependences of R_1 and MPF in WM and GM on the B_1 scaling factor c in the absence of B_1 correction and after surrogate B_1 field correction for the optimized protocol are presented in Fig. 2. Relative errors before and after surrogate B_1 correction and the effect of variations in the algorithm coefficients r_0 and r_f are illustrated in Fig. 3. In agreement with the literature [4], B_1 -related errors result in an inverse quadratic dependence of R_1 with a four-fold overestimation (300% relative error) at $c = 0.5$ (Fig. 2(a), 3(a), and 3(b)). The B_1 dependence of MPF is nearly linear with the errors being in a range from -25% to $+35\%$ for c varying from 1.5 to 0.5 (Fig. 2(b), 3(c), and 3(d)). Analytical formulas for B_1 -related errors (15) and (17) provide accurate approximations of the numerical simulations (Fig. 2). It is also important to emphasize that the relative errors for WM and GM appear very similar (Fig. 3), thus confirming their negligible dependence on the tissue parameters in accordance with the analytical approximations (15) and (18).

Application of the surrogate field correction algorithm with the accurate values of the coefficients r_0 and r_f results in

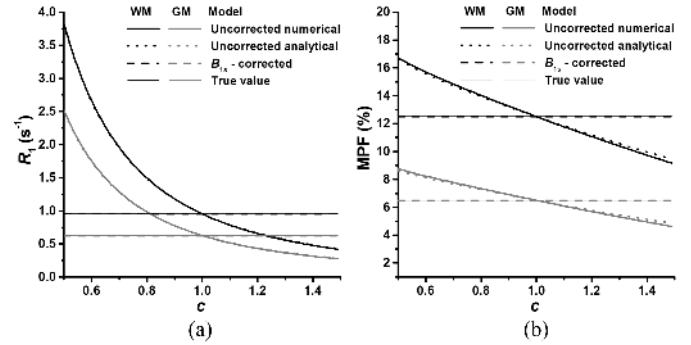


Fig. 2. Simulated dependences of R_1 (a) and MPF (b) measurements on the B_1 scaling factor before (solid and dot lines) and after (dash lines) correction using the surrogate B_1 field estimation algorithm for the sequence parameters from the high-resolution research protocol and tissue parameters corresponding to WM (black lines) and GM (gray lines). Uncorrected R_1 (a) and MPF (b) values were simulated either numerically (solid lines) or analytically using (15) and (17) (dot lines). Thin solid lines correspond to the R_1 (a) and MPF (b) values in the absence of B_1 inhomogeneity ($c = 1$).

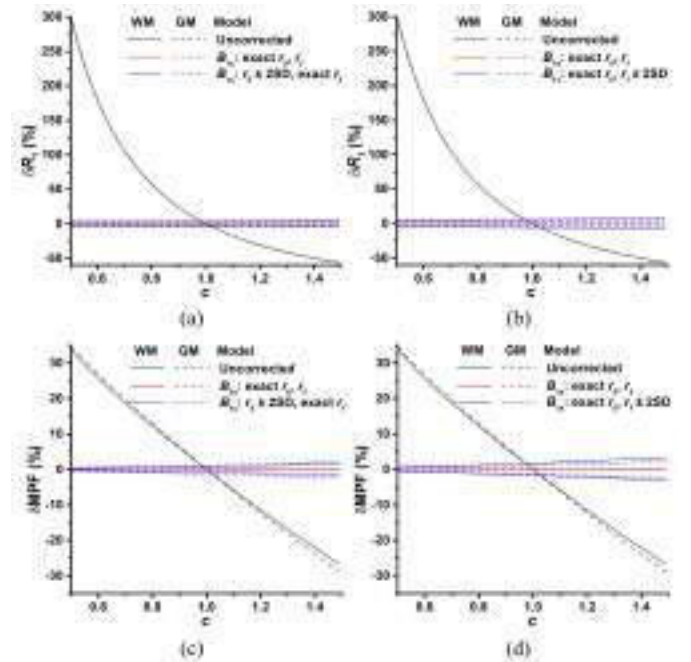


Fig. 3. Simulated relative errors of surrogate B_1 field correction in R_1 (a, b) and MPF (c, d) caused by uncertainties in the algorithm coefficients r_0 (a, c) and r_f (b, d). Relative errors in each parameter are plotted for WM (solid lines) and GM (dashed lines) as functions of the B_1 scaling factor for the following settings: the absence of correction (black lines), correction with exact r_0 and r_f values (red lines), and correction with either r_0 or r_f deviating by $\pm 2\text{SD}$ from its exact value (blue lines). Simulations are presented for the sequence parameters from the high-resolution research protocol.

nearly complete elimination of B_1 -related errors from R_1 and MPF (Fig. 2 and 3). Potential errors of the algorithm associated with inaccuracy of the constants r_0 and r_f were simulated under assumption of their variations within the range of $\pm 2\text{SD}$ of the experimental measurements given above. The corresponding residual errors in R_1 and MPF appeared rather small ($< 10\%$ for R_1 and $< 5\%$ for MPF, Fig. 3), being substantially less than B_1 -related errors without correction for a wide range

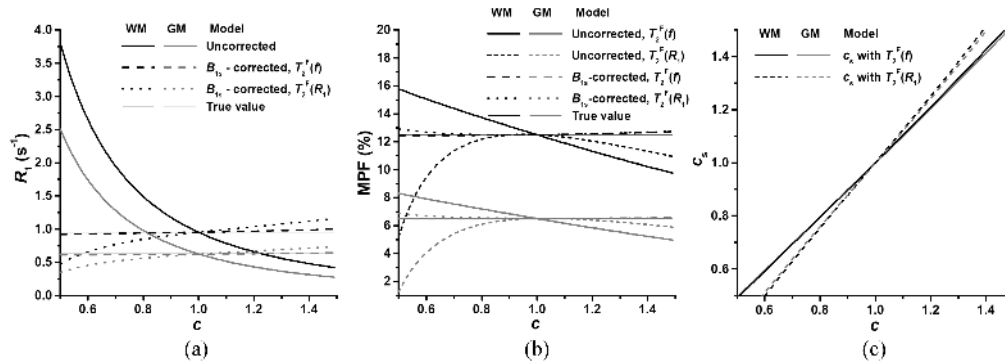


Fig. 4. Simulated dependences of the uncorrected (solid and short-dash lines) and corrected with surrogate B_1 field (dash and dot lines) R_1 (a) and MPF (b) measurements and the surrogate B_1 field scaling factor c_s (c) on the actual B_1 scaling factor for the sequence parameters from the prototype clinical protocol and tissue parameters corresponding to WM (black lines) and GM (gray lines). Simulations are presented for the two parameterizations of the direct saturation effect in the single-point MPF fitting algorithm based on either MPF-related formula (24) or the constant product $R_1 T_2^F$. The parameterization with (24) results in the uncorrected MPF (b) and c_s (c) dependences plotted by solid lines and the corrected R_1 (a) and MPF (b) dependences plotted by dash lines. The parameterization with the constant product $R_1 T_2^F$ results in the uncorrected MPF (b) and c_s (c) dependences plotted by short-dash lines and the corrected R_1 (a) and MPF (b) dependences plotted by dot lines. Thin solid lines correspond to the R_1 (a) and MPF (b) values in the absence of B_1 inhomogeneity ($c = 1$).

of B_1 non-uniformities. It should be noted that if either r_0 or r_f deviates from its exact value, the corresponding error in the surrogate B_1 field estimate c_s (23) becomes dependent on the actual field scaling factor c . These dependences are nearly linear and rather weak (data are not shown). For the simulations presented in Fig. 3, the absolute error in c_s varies from ± 0.01 at $c \approx 0.5$ to ± 0.05 at $c \approx 1.5$. The errors in c_s translate differently into the corresponding errors in R_1 and MPF. For R_1 , the relative errors are nearly constant across the entire range of c_s values (Fig. 3(a) and 3(b)), whereas the MPF errors replicate the linear trend in c_s (Fig. 3(c) and 3(d)). Such a behavior of errors can be easily proven by the analysis of approximated equations (15) and (22). Uncertainties in the coefficients r_0 or r_f may introduce additional errors in corrected maps as compared to the uncorrected case, if B_1 field is uniform. As seen in Fig. 3, the errors without surrogate B_1 correction in the vicinity of $c = 1$ (c in a range of 0.95-1.05) can be smaller than the errors caused by variations in r_0 or r_f . Accordingly, if uncertainties in the coefficients r_0 and r_f are assumed to vary within $\pm 2SD$, the simulations suggest that the algorithm is expected to improve accuracy of both R_1 and MPF measurements for B_1 inhomogeneities exceeding $\pm 5\%$. Conversely, the utility of the proposed method may be limited in the applications with a smaller range of B_1 variations.

Fig. 4 illustrates the rationale for reparameterization of the direct saturation effect described above. Simulations were performed with the listed above parameters of the clinical sequence, which is characterized by a relatively small offset frequency and, therefore, more prone to the errors associated with direct saturation of the free pool. The model based on the constant product $R_{1m} T_2^F$ results in a non-monotonic behavior of B_1 -related errors in MPF (Fig. 4(b)), which translates in inaccurate estimation of surrogate B_1 field (Fig. 4(c)). Correspondingly, correction of both R_1 and MPF with this parameterization appears substantially inaccurate for large B_1 non-uniformities (Fig. 4(a) and 4(b)). In contrast, new parameterization (24) eliminates this problem and results in both close agreement between the actual and surrogate B_1

non-uniformity factors (Fig. 4(c)) and accurate correction of R_1 and MPF values in a wide range of B_1 inhomogeneities (Fig. 4(a) and 4(b)).

C. Experimental Comparison Between Actual and Surrogate B_1 Corrections

An example of the application of the surrogate B_1 field correction algorithm to a dataset obtained with the high-resolution 3D R_1 and MPF mapping protocol is presented in Fig. 5. Uncorrected R_1 and MPF (Fig. 5(a) and 5(b)) demonstrate large B_1 -dependent variations, as seen in the difference images (Fig. 5(i) and 5(j)) obtained by their subtraction from the maps reconstructed with actual B_{1a} correction (Fig. 5(c) and 5(d)). The surrogate B_{1s} map (Fig. 5(h)) reconstructed from uncorrected R_1 and MPF maps shows a very similar pattern of B_1 non-uniformity to that observed in the actual B_{1a} map (Fig. 5(g)). The R_1 and MPF maps corrected by applying surrogate B_{1s} field (Fig. 5(e) and 5(f)) demonstrate close agreement with the maps reconstructed using actual B_{1a} correction, as evidenced by their subtraction images (Fig. 5(k) and 5(l)), which show minor residual variability.

More detailed examination of the residual errors of surrogate B_1 correction using percentage difference maps (Fig. 5(n), 5(o), and 5(p)) suggests that local discrepancies in R_1 and MPF (Fig. 5(n) and 5(o)) closely reproduce the patterns of the difference between the actual and surrogate B_1 scaling factors (Fig. 5(m)) but have different quantitative scales. Local percentage errors across the brain parenchyma varied in ranges of about ± 10 -12% for R_1 (Fig. 5(n)), ± 2 -3% for MPF (Fig. 5(o)), and ± 5 -6% for B_1 (Fig. 5(p)). These errors appeared in good agreement with the simulation results presented in Fig. 3. Larger negative errors (up to -20% for R_1 , -6% for MPF, and -10% for B_1) were observed at certain locations on the brain boundary and around the frontal pole. The patterns of local errors exemplified in Fig. 5 were consistent across all datasets. Anatomic locations of the most discrepant regions suggest that the largest errors of

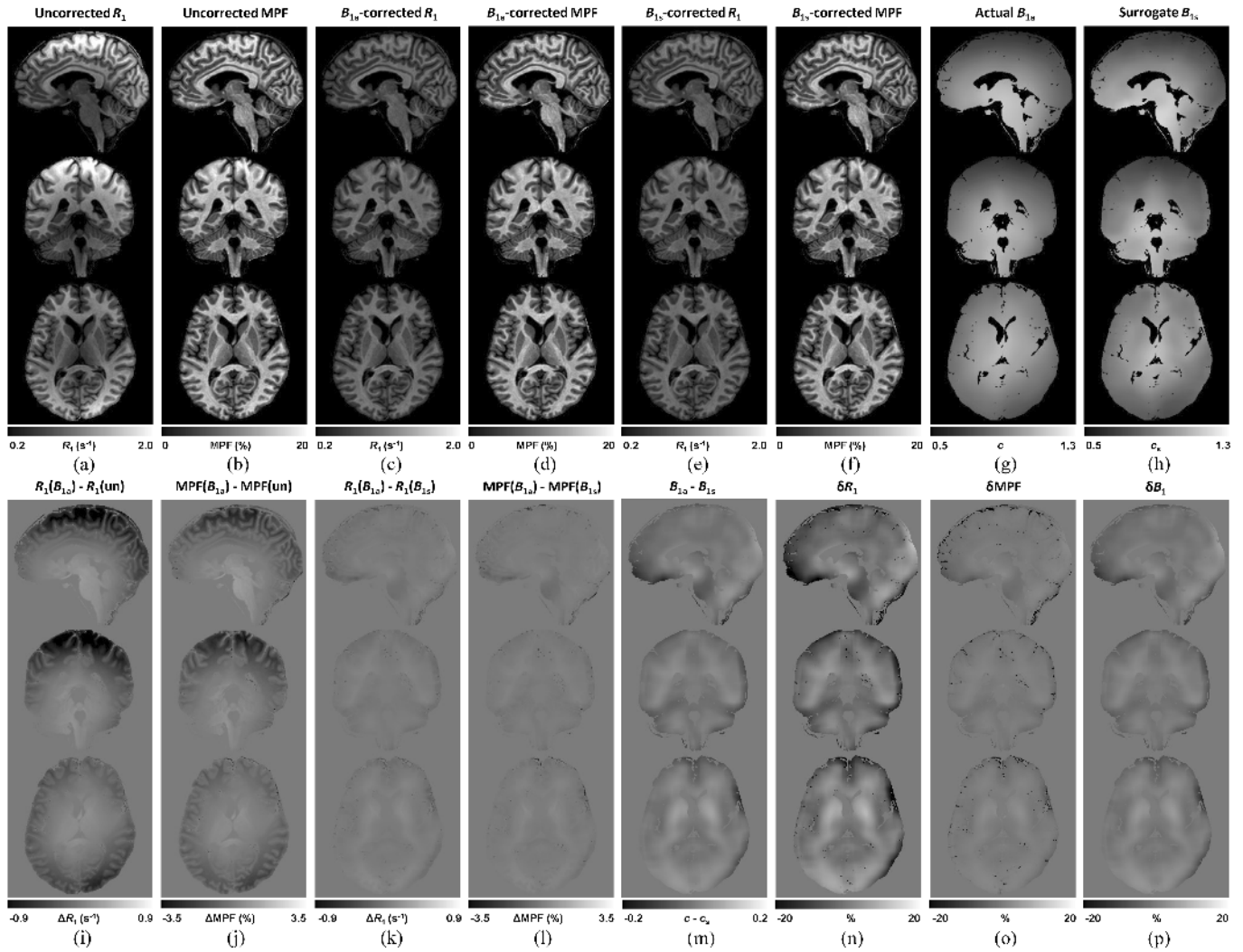


Fig. 5. Example application of the surrogate B_1 field correction algorithm to high-resolution 3D R_1 and MPF maps. 3D cross-sections show uncorrected R_1 (a) and MPF (b) maps; corrected with actual B_1 (B_{1a}) field R_1 (c) and MPF (d) maps; corrected with surrogate B_1 (B_{1s}) field R_1 (e) and MPF (f) maps; B_{1a} (g) and B_{1s} (h) field maps; subtraction images between the corrected with actual B_{1a} field and uncorrected R_1 (i) and MPF (j) maps; subtraction images between the corrected with actual B_{1a} and surrogate B_{1s} fields R_1 (k) and MPF (l) maps; difference between actual and surrogate B_1 maps (m); maps of residual percentage errors in R_1 (n) and MPF (o) after surrogate B_1 correction; and a percentage error map of surrogate B_1 field estimation (p).

surrogate B_1 correction may be associated with substantial non-uniformities of B_0 field, proximity of large blood vessels, or sub-voxel misregistration between high-resolution source images and a low-resolution actual B_1 map.

Voxel-wise agreement between actual and surrogate B_1 correction is illustrated by the voxel-based individual Bland-Altman plots for the B_1 field scaling factor, MPF, and R_1 (Fig. 6 and Supplementary Material), and the summary of their analysis given in Table I. In all datasets, Bland-Altman analysis showed no significant bias and relatively narrow limits of agreement (Table I). Both limits of agreement and voxel-based coefficients of variations (Table I) suggest that MPF is characterized by the smallest residual correction errors, followed by B_1 and R_1 . In the relative scale, the voxel-based limits of agreement indicate that residual deviations for 95% of voxels do not exceed $\pm 11\%$ for R_1 , $\pm 3\%$ for MPF, and $\pm 6\%$ for the B_1 scaling factor. These estimates are in close

correspondence with the observations from percentage error maps (Fig. 5) and simulations (Fig. 3).

Mean R_1 and MPF values in segmented brain tissues across 11 study participants and statistical comparisons between the parameter measurements obtained with actual and surrogate B_1 correction and without correction are presented in Table II. Bland-Altman plots exemplifying the effect of surrogate B_1 field correction on R_1 and MPF measurements in brain tissues are shown in Fig. 7. In the absence of B_1 correction, the mean R_1 and MPF values in WM, GM, and PVCSF demonstrate highly-significant biases relative to the measurements corrected using the actual B_1 maps (Table II, Fig. 7(a) and 7(c)). Application of the surrogate B_1 field correction algorithm reduced the biases in both R_1 and MPF to a non-significant level for all tissues (Table II, Fig. 7(b) and 7(d)). Surrogate B_1 correction also dramatically reduced the coefficients of variation (Table II).

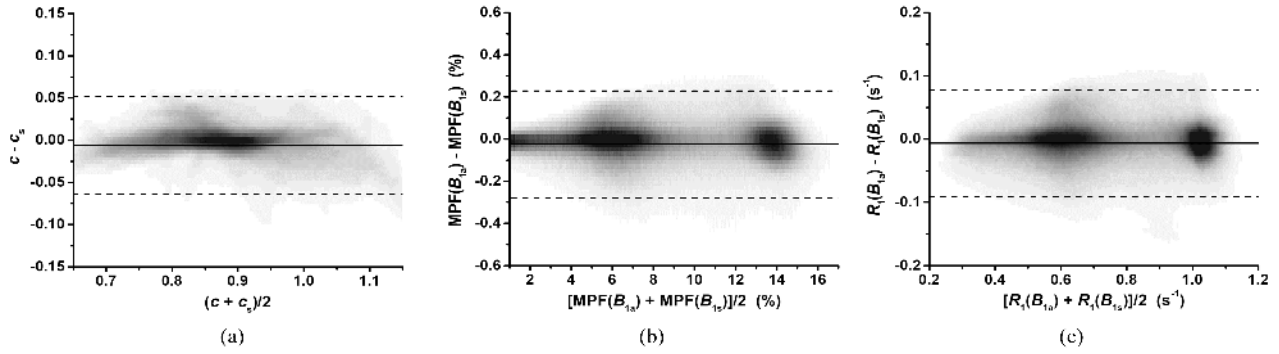


Fig. 6. Example voxel-based Bland-Altman plots for a single study participant illustrating an agreement between the actual and surrogate B_1 field scaling factors (a), the MPF maps corrected with actual and surrogate B_1 field (b), and the R_1 maps corrected with actual and surrogate B_1 field (c). Solid and dashed lines correspond to the mean difference and limits of agreement calculated from all non-zero voxels in the 3D maps. Grayscale (from white to black) represents voxel density ranges 0–0.15% for B_1 maps, 0–0.02% for MPF maps, and 0–0.04% for R_1 maps.

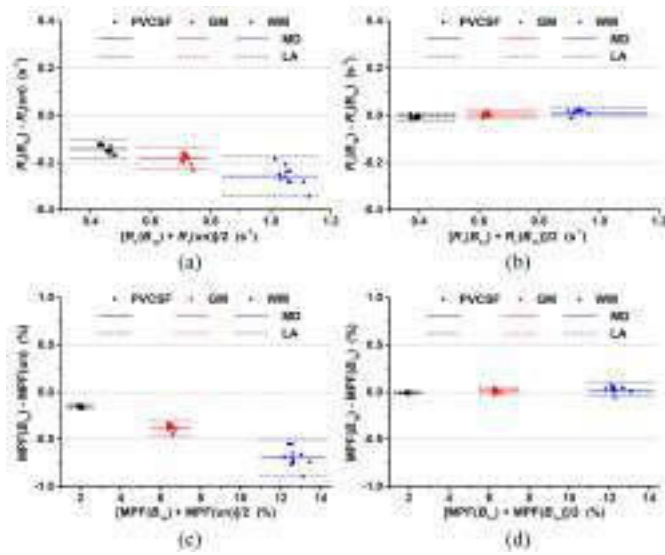


Fig. 7. Bland-Altman plots comparing R_1 (a, b) and MPF (c, d) measurements in segmented brain tissues between reconstructions with actual B_{1a} field correction and without correction (a, c) and between reconstructions with actual B_{1a} and surrogate B_{1s} field corrections (b, d). Black, red, and blue colors correspond to the PVCSP, GM, and WM tissue classes, respectively. Solid and dash lines indicate mean differences (MD) and limits of agreement (LA).

D. Compatibility With Clinical MRI Sequences

Application of the surrogate B_1 correction algorithm to the R_1 and MPF mapping dataset obtained using unmodified manufacturer's pulse sequences is demonstrated in Fig. 8. The surrogate B_{1s} field map (Fig. 8(a)) shows substantial similarity to the actual B_{1a} distribution, as seen in the subtraction $B_{1a} - B_{1s}$ image (Fig. 8(f)). The only notable distinction is some B_1 underestimation by the surrogate field map in the proximity to paranasal sinuses (Fig. 8(a) and 8(f)), which may be attributed to high B_0 inhomogeneity in this area. Despite this discrepancy, large B_1 -dependent deviations in uncorrected MPF (Fig. 8(b) and 8(g)) and R_1 (Fig. 8(d) and 8(i)) maps are effectively eliminated by surrogate B_{1s} correction (Fig. 8(c), 8(e), 8(h), and 8(j)). Corresponding subtraction images calculated as the difference between the maps reconstructed with actual B_{1a} and surrogate B_{1s} corrections

TABLE I

MEAN STATISTICAL METRICS FOR VOXEL-BASED BLAND-ALTMAN PLOTS COMPARING ACTUAL AND SURROGATE B_1 FIELD CORRECTION

Metric	B_1 (c or c_s)	MPF (%)	R_1 (s^{-1})
B_{1a} mean	0.897 ± 0.017	7.90 ± 0.46	0.712 ± 0.014
B_{1s} mean	0.896 ± 0.018	7.90 ± 0.45	0.710 ± 0.013
Bias	0.001 ± 0.006	0.00 ± 0.02	0.002 ± 0.009
SD of Bias	0.028 ± 0.003	0.11 ± 0.01	0.040 ± 0.004
Limits of	-0.055 ± 0.009	-0.22 ± 0.04	-0.077 ± 0.012
Agreement	0.056 ± 0.006	0.23 ± 0.03	0.081 ± 0.011
Voxel-based	2.23 ± 0.26	1.14 ± 0.10	4.33 ± 0.42
CoV (%)			

Note: All data are presented as the mean \pm SD across 12 study participants.

(Fig. 8(h) and 8(j)) demonstrate remarkable uniformity with minor propagation of the above-mentioned artefact into the R_1 map (Fig. 8(j)).

V. DISCUSSION

This study introduces a new data-driven retrospective algorithm for correction of B_1 -related errors in quantitative imaging. The described algorithm uses actually measured VFA R_1 and single-point MPF maps to derive an approximated B_1 field map based on the rigorous analytical theory. The presented results indicate that the application of surrogate B_1 field enables accurate correction of R_1 and MPF maps across a wide range of B_1 non-uniformities and native R_1 and MPF values in tissues.

The primary area of use of the described algorithm is B_1 correction in the single-point MPF mapping method [5], [6]. This method becomes increasingly popular over the past years as a fast and reliable tool for quantitative myelin mapping in pre-clinical and clinical neuroscience [7]–[17], [23], [24]. The need for correction of B_1 -related errors constitutes the major obstacle in routine applications of fast MPF mapping, especially in high magnetic fields. While not as large as errors in R_1 , these errors require correction even at the level of global brain tissue analysis due to a statistically significant bias they introduce [17]. The common practice in current

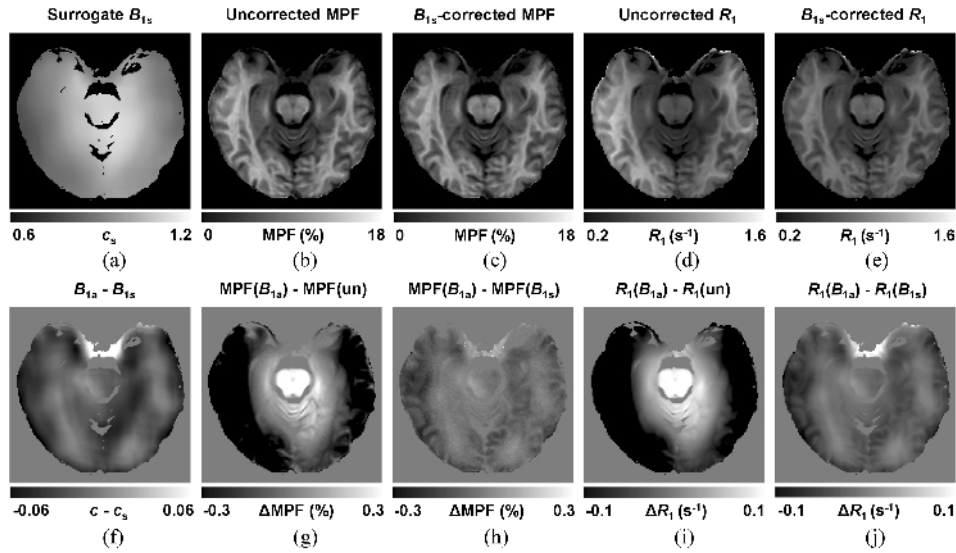


Fig. 8. Application of the surrogate B_1 field correction algorithm to the R_1 and MPF maps obtained using clinical imaging sequences. A cross-section at the midbrain level shows the surrogate B_{1s} map (a); uncorrected (b) and corrected with B_{1s} field (c) MPF maps; uncorrected (d) and corrected with B_{1s} field (e) R_1 maps; subtraction image between the actual B_{1a} and surrogate B_{1s} maps (f); subtraction image between the corrected with actual B_{1a} field and uncorrected MPF maps (g); subtraction image between the MPF maps corrected with actual B_{1a} and surrogate B_{1s} fields (h); subtraction image between the corrected with actual B_{1a} field and uncorrected R_1 maps (i); and subtraction image between the R_1 maps corrected with actual B_{1a} and surrogate B_{1s} fields (j).

TABLE II
COMPARISONS BETWEEN CORRECTED WITH ACTUAL AND SURROGATE B_1 FIELDS
AND UNCORRECTED R_1 AND MPF IN SEGMENTED BRAIN TISSUES

Value	R_1 (s^{-1})			MPF (%)		
	WM	GM	PVCSF	WM	GM	PVCSF
Uncorrected mean \pm SD	1.187 \pm 0.051	0.809 \pm 0.022	0.526 \pm 0.027	13.04 \pm 0.39	6.71 \pm 0.13	2.08 \pm 0.10
B_{1a} corrected mean \pm SD	0.930 \pm 0.021	0.626 \pm 0.009	0.384 \pm 0.012	12.34 \pm 0.34	6.33 \pm 0.11	1.92 \pm 0.09
B_{1s} corrected mean \pm SD	0.918 \pm 0.019	0.622 \pm 0.008	0.390 \pm 0.011	12.32 \pm 0.35	6.32 \pm 0.12	1.93 \pm 0.09
Bias B_{1a} -Uncorrected \pm SD	-0.257 \pm 0.042	-0.183 \pm 0.023	-0.143 \pm 0.018	-0.70 \pm 0.10	-0.38 \pm 0.04	-0.16 \pm 0.01
(P)	(<0.001)	(<0.001)	(<0.001)	(<0.001)	(<0.001)	(<0.001)
Bias B_{1a} - B_{1s} \pm SD	0.012 \pm 0.009	0.003 \pm 0.008	-0.007 \pm 0.007	0.02 \pm 0.03	0.01 \pm 0.02	-0.01 \pm 0.01
(P)	(0.49)	(0.83)	(0.35)	(0.57)	(0.57)	(0.09)
CoV B_{1a} -Uncorrected (%)	17.4	18.2	22.4	3.9	4.2	5.7
CoV B_{1a} - B_{1s} (%)	1.2	1.0	1.8	0.2	0.2	0.4
ANOVA F (P)	424 (<0.001)	664 (<0.001)	569 (<0.001)	551 (<0.001)	956 (<0.001)	1140 (<0.001)

fast MPF mapping applications in magnetic fields of 3 T and higher is to map B_1 field using specialized sequences, which typically add 2-5 minutes to the examination time, if a B_1 map is required to provide continuous 3D whole-brain coverage and sufficient resolution for correction of quantitative MPF and R_1 maps. Also, the majority of advanced B_1 mapping techniques are based on customized pulse sequences and unavailable to users of routine clinical MRI equipment. Retrospective correction of B_1 non-uniformity during post-processing provides an attractive alternative solution of the above problem. While no post-processing method has been proposed to specifically correct errors caused by B_1 , more general non-uniformity correction algorithms based on bias-field

reconstruction can be applied to quantitative parametric maps [31]–[33]. If B_1 distribution is the main source of low-frequency intensity variations, such as in R_1 maps, bias field can be viewed as a proxy of B_1 field [31], [32]. However, a general limitation of all bias field correction approaches is their non-quantitative nature. Particularly, the earlier bias field correction technique for R_1 mapping [31] relies on the assumption of unbiased global B_1 calibration, which is not always correct, as indicated by the systematic deviation of whole-brain B_1 values from unity ($c \approx 0.9$, Table I) found in the present study. Another approach [32] is based on the assumption of a constant T_1 in a reference tissue, which is used to extract global flip angle calibration. This assumption

may not hold due to tissue changes caused by age or disease and variability in the definition of reference anatomic regions. In contrast to alternative approaches, the proposed surrogate B_1 correction algorithm eliminates the need for acquisition of separate B_1 maps and provides unbiased quantitative R_1 and MPF measurements based on a simple post-processing procedure.

Besides MPF mapping, the described algorithm demonstrated reasonable performance in correction of R_1 maps. Accordingly, it potentially can be used to correct B_1 -related errors in R_1 maps alone, if R_1 or T_1 is a primary parameter of interest. In such a prospective application, an MT-weighted image can provide supplementary data for reconstruction of a surrogate B_1 field map instead of any B_1 mapping sequence. An attractive feature of this technique is the broad availability of MT-weighted sequences on clinical MRI systems. Additionally, the described algorithm potentially can be combined with multi-parameter quantitative MT techniques utilizing VFA data for R_1 estimation [18], [19], [34] and an empirical approach to quantify MT saturation, R_1 , and PD using three GRE source images [35].

Accuracy of the described algorithm depends on the correct values of the regression coefficients r_0 and r_f , which should match particular experimental settings and an MPF reconstruction model. Since R_1 strongly depends on magnetic field strength, whereas MPF is independent of magnetic field [23], [24], the values of r_0 and r_f are expected to have a similar to R_1 field dependence. To a lesser extent, the algorithm constants may be influenced by certain instrumental factors not accounted by the VFA and MPF reconstruction models, such as imperfect spoiling [25] or finite duration of excitation pulses [36]. Due to variations in the sequence design between MRI systems of different manufacturers, the optimal values of r_0 and r_f may be platform-dependent. The coefficients r_0 and r_f may also be affected by some modifications of the MT signal model. Examples of such modifications include different assumptions about R_1 of macromolecular protons [37], [38], correction of bi-exponential biases in R_1 and MPF [39], inclusion of a non-exchangeable water compartment [40], and different parameterizations to constrain T_2^F discussed above. Until more experience is gained in applications of the surrogate B_1 correction method, it would be advisable to measure the coefficients r_0 and r_f for a particular MRI system, protocol, and reconstruction software in a pilot series of experiments with actual B_1 mapping as a gold standard.

Certain limitations of the surrogate B_1 field mapping algorithm should be noted. First, an object under investigation must exhibit a significant MT effect enabling a non-zero estimate of MPF. Consequently, the method cannot be used for tissues with a negligible MT effect, such as cerebrospinal fluid or fat [41], as well as for fluid-filled phantoms. Second, the algorithm may result in incorrect surrogate B_1 field estimation in certain tissues, for which the relationship between R_1 and MPF strongly deviates from the linear form (21). This situation may occur due to substantial T_1 shortening caused by the paramagnetic effect, particularly in enhancing lesions after administration of a contrast agent, hemorrhages, or tissues with excessive iron deposition. For such special

cases, additional post-processing approaches may be needed, for example, lesion masking followed by interpolation of surrogate B_1 field. Third, for clinical MT sequences with low saturation offset frequency, some influence of B_0 inhomogeneities may be expected. While the effect of B_0 on MPF measurements was demonstrated to be negligibly small for optimal protocol settings [17], it may be more pronounced for clinical MT sequences in the anatomic regions with large B_0 non-uniformity, particularly, in the brain areas proximal to paranasal sinuses or in the presence of metallic implants. More research is needed to evaluate practical importance of this potential limitation. Fourth, the MT model used in this study does not explicitly include the dependence of R_1 on cross-relaxation parameters [39], [42], which may affect both R_1 [39], [42] and MPF [39] estimates. Theoretically, this effect can be incorporated into the proposed algorithm in future studies with the use of recalculation formulas described elsewhere [39]. Finally, the application of the described method to non-brain tissues remains a topic of future studies. Such applications, while generally possible, would require knowledge of the two-pool MT model parameters and coefficients r_0 and r_f for particular organs and tissues of interest.

In conclusion, this study demonstrated and validated a new data-driven approach for accurate correction of errors caused by B_1 field non-uniformity in VFA R_1 and single-point MPF mapping of the human brain. The described surrogate B_1 field correction algorithm obviates the use of dedicated B_1 mapping sequences in fast MPF mapping, thus enhancing time-efficiency and availability of this increasingly popular quantitative myelin imaging technology. This algorithm may also provide an alternative solution for correction of B_1 non-uniformities in VFA R_1 mapping applications by replacing a B_1 mapping sequence with an MT-weighted scan. Future research is needed to expand the applicability of the surrogate B_1 field correction method to non-brain tissues.

REFERENCES

- [1] P. S. Tofts, "Measurement process: MR data collection and image analysis," in *Quantitative MRI of the Brain: Principles of Physical Measurement*, 2nd ed., M. Cercignani, N. G. Dowell, and P. S. Tofts, Eds. Boca Raton, FL, USA: CRC Press, 2018, pp. 13–32.
- [2] E. K. Fram *et al.*, "Rapid calculation of T1 using variable flip angle gradient refocused imaging," *Magn. Reson. Imag.*, vol. 5, no. 3, pp. 201–208, Jan. 1987.
- [3] S. C. L. Deoni, T. M. Peters, and B. K. Rutt, "High-resolution T1 and T2 mapping of the brain in a clinically acceptable time with DESPOT1 and DESPOT2," *Magn. Reson. Med.*, vol. 53, no. 1, pp. 237–241, Jan. 2005.
- [4] G. Helms, H. Dathe, and P. Dechent, "Quantitative FLASH MRI at 3T using a rational approximation of the Ernst equation," *Magn. Reson. Med.*, vol. 59, no. 3, pp. 667–672, Mar. 2008.
- [5] V. L. Yarnykh, "Fast macromolecular proton fraction mapping from a single off-resonance magnetization transfer measurement," *Magn. Reson. Med.*, vol. 68, no. 1, pp. 166–178, Jul. 2012.
- [6] V. L. Yarnykh, "Time-efficient, high-resolution, whole brain three-dimensional macromolecular proton fraction mapping," *Magn. Reson. Med.*, vol. 75, no. 5, pp. 2100–2106, May 2016.
- [7] H. R. Underhill, R. C. Rostomily, A. M. Mikheev, C. Yuan, and V. L. Yarnykh, "Fast bound pool fraction imaging of the *in vivo* rat brain: Association with myelin content and validation in the C6 glioma model," *NeuroImage*, vol. 54, No. 3, pp. 2052–2065, Feb. 2011.
- [8] M. Y. Khodanovich *et al.*, "Histological validation of fast macromolecular proton fraction mapping as a quantitative myelin imaging method in the cuprizone demyelination model," *Sci. Rep.*, vol. 7, no. 1, Apr. 2017, Art. no. 46686.

- [9] M. Y. Khodanovich *et al.*, "Quantitative assessment of demyelination in ischemic stroke *in vivo* using macromolecular proton fraction mapping," *J. Cerebral Blood Flow Metabolism*, vol. 38, no. 5, pp. 919–931, May 2018.
- [10] Khodanovich *et al.*, "Quantitative imaging of white and gray matter remyelination in the cuprizone demyelination model using the macromolecular proton fraction," *Cells*, vol. 8, no. 10, p. 1204, Oct. 2019.
- [11] V. L. Yarnykh *et al.*, "Fast whole-brain three-dimensional macromolecular proton fraction mapping in multiple sclerosis," *Radiology*, vol. 274, no. 1, pp. 210–220, Jan. 2015.
- [12] V. L. Yarnykh *et al.*, "Iron-insensitive quantitative assessment of sub-cortical gray matter demyelination in multiple sclerosis using the macromolecular proton fraction," *Amer. J. Neuroradiol.*, vol. 39, no. 4, pp. 618–625, Apr. 2018.
- [13] E. C. Petrie *et al.*, "Neuroimaging, behavioral, and psychological sequelae of repetitive combined blast/impact mild traumatic brain injury in Iraq and Afghanistan war veterans," *J. Neurotrauma*, vol. 31, no. 5, pp. 425–436, Mar. 2014.
- [14] V. L. Yarnykh, I. Y. Prihod'ko, A. A. Savelov, and A. M. Korostyshevskaya, "Quantitative assessment of normal fetal brain myelination using fast macromolecular proton fraction mapping," *Amer. J. Neuroradiol.*, vol. 39, no. 7, pp. 1341–1348, Jul. 2018.
- [15] A. M. Korostyshevskaya, A. A. Savelov, L. I. Papusha, A. E. Druy, and V. L. Yarnykh, "Congenital medulloblastoma: Fetal and postnatal longitudinal observation with quantitative MRI," *Clin. Imag.*, vol. 52, pp. 172–176, Nov. 2018.
- [16] A. M. Korostyshevskaya, I. Y. Prihod'ko, A. A. Savelov, and V. L. Yarnykh, "Direct comparison between apparent diffusion coefficient and macromolecular proton fraction as quantitative biomarkers of the human fetal brain maturation," *J. Magn. Reson. Imag.*, vol. 50, no. 1, pp. 52–61, Jul. 2019.
- [17] V. L. Yarnykh, A. A. Kisel, and M. Y. Khodanovich, "Scan-rescan repeatability and impact of B_0 and B_1 field nonuniformity corrections in single-point whole-brain macromolecular proton fraction mapping," *J. Magn. Reson. Imag.*, vol. 51, no. 6, pp. 1789–1798, Jun. 2020.
- [18] V. L. Yarnykh, "Pulsed Z-spectroscopic imaging of cross-relaxation parameters in tissues for human MRI: Theory and clinical applications," *Magn. Reson. Med.*, vol. 47, no. 5, pp. 929–939, May 2002.
- [19] V. L. Yarnykh and C. Yuan, "Cross-relaxation imaging reveals detailed anatomy of white matter fiber tracts in the human brain," *NeuroImage*, vol. 23, no. 1, pp. 409–424, Sep. 2004.
- [20] C. Morrison and R. M. Henkelman, "A model for magnetization transfer in tissues," *Magn. Reson. Med.*, vol. 33, no. 4, pp. 475–482, Apr. 1995.
- [21] G. J. Stanisz *et al.*, " T_1 , T_2 relaxation and magnetization transfer in tissue at 3T," *Magn. Reson. Med.*, vol. 54, no. 3, pp. 507–512, Sep. 2005.
- [22] M. F. Callaghan, G. Helms, A. Lutti, S. Mohammadi, and N. Weiskopf, "A general linear relaxometry model of R_1 using imaging data," *Magn. Reson. Med.*, vol. 73, no. 3, pp. 1309–1314, Mar. 2015.
- [23] A. V. Naumova, A. E. Akulov, M. Y. Khodanovich, and V. L. Yarnykh, "High-resolution three-dimensional macromolecular proton fraction mapping for quantitative neuroanatomical imaging of the rodent brain in ultra-high magnetic fields," *NeuroImage*, vol. 147, pp. 985–993, Feb. 2017.
- [24] N. V. Anisimov, O. S. Pavlova, Y. A. Pirogov, and V. L. Yarnykh, "Three-dimensional fast single-point macromolecular proton fraction mapping of the human brain at 0.5 Tesla," *Quant. Imag. Med. Surgery*, vol. 10, no. 7, pp. 1441–1449, Jul. 2020.
- [25] V. L. Yarnykh, "Optimal radiofrequency and gradient spoiling for improved accuracy of T_1 and B_1 measurements using fast steady-state techniques," *Magn. Reson. Med.*, vol. 63, no. 6, pp. 1610–1626, Jun. 2010.
- [26] V. L. Yarnykh, "Actual flip-angle imaging in the pulsed steady state: A method for rapid three-dimensional mapping of the transmitted radiofrequency field," *Magn. Reson. Med.*, vol. 57, no. 1, pp. 192–200, Jan. 2007.
- [27] K. P. Pruessmann, M. Weiger, M. B. Scheidegger, and P. Boesiger, "SENSE: Sensitivity encoding for fast MRI," *Magn. Reson. Med.*, vol. 42, no. 5, pp. 952–962, Nov. 1999.
- [28] G. Helms and P. Dechent, "Increased SNR and reduced distortions by averaging multiple gradient echo signals in 3D FLASH imaging of the human brain at 3T," *J. Magn. Reson. Imag.*, vol. 29, no. 1, pp. 198–204, Jan. 2009.
- [29] S. M. Smith, "Fast robust automated brain extraction," *Hum. Brain Mapping*, vol. 17, no. 3, pp. 143–155, Nov. 2002.
- [30] Y. Zhang, M. Brady, and S. Smith, "Segmentation of brain MR images through a hidden Markov random field model and the expectation-maximization algorithm," *IEEE Trans. Med. Imag.*, vol. 20, no. 1, pp. 45–57, Jan. 2001.
- [31] N. Weiskopf, A. Lutti, G. Helms, M. Novak, J. Ashburner, and C. Hutton, "Unified segmentation based correction of R_1 brain maps for RF transmit field inhomogeneities (UNICORT)," *NeuroImage*, vol. 54, no. 3, pp. 2116–2124, Feb. 2011.
- [32] G. Liberman, Y. Louzoun, and D. Ben Bashat, "T1 mapping using variable flip angle SPGR data with flip angle correction," *J. Magn. Reson. Imag.*, vol. 40, no. 1, pp. 171–180, Jul. 2014.
- [33] S. Volz, U. Nöth, and R. Deichmann, "Correction of systematic errors in quantitative proton density mapping," *Magn. Reson. Med.*, vol. 68, no. 1, pp. 74–85, Jul. 2012.
- [34] M. Boudreau, N. Stikov, and G. B. Pike, " B_1 -sensitivity analysis of quantitative magnetization transfer imaging," *Magn. Reson. Med.*, vol. 79, no. 1, pp. 228–276, Jan. 2018.
- [35] G. Helms, H. Dathe, K. Kallenberg, and P. Dechent, "High-resolution maps of magnetization transfer with inherent correction for RF inhomogeneity and T_1 relaxation obtained from 3D FLASH MRI," *Magn. Reson. Med.*, vol. 60, no. 6, pp. 1396–1407, Dec. 2008.
- [36] N. Boulant, " T_1 and T_2 effects during radio-frequency pulses in spoiled gradient echo sequences," *J. Magn. Reson.*, vol. 197, no. 2, pp. 213–218, Apr. 2009.
- [37] G. Helms and G. E. Hagberg, "In vivo quantification of the bound pool T_1 in human white matter using the binary spin-bath model of progressive magnetization transfer saturation," *Phys. Med. Biol.*, vol. 54, no. 23, pp. N529–N540, Dec. 2009.
- [38] P. van Gelderen, X. Jiang, and J. H. Duyn, "Rapid measurement of brain macromolecular proton fraction with transient saturation transfer MRI," *Magn. Reson. Med.*, vol. 77, no. 6, pp. 2174–2185, Jun. 2017.
- [39] P. Mossahebi, V. L. Yarnykh, and A. Samsonov, "Analysis and correction of biases in cross-relaxation MRI due to biexponential longitudinal relaxation," *Magn. Reson. Med.*, vol. 71, no. 2, pp. 830–838, Feb. 2014.
- [40] P. Mossahebi, A. L. Alexander, A. S. Field, and A. A. Samsonov, "Removal of cerebrospinal fluid partial volume effects in quantitative magnetization transfer imaging using a three-pool model with nonexchanging water component," *Magn. Reson. Med.*, vol. 74, no. 5, pp. 1317–1326, Nov. 2015.
- [41] A. Samsonov, F. Liu, and J. V. Velikina, "Resolving estimation uncertainties of chemical shift encoded fat-water imaging using magnetization transfer effect," *Magn. Reson. Med.*, vol. 82, no. 1, pp. 202–212, Jul. 2019.
- [42] R. P. A. G. Teixeira, S. J. Malik, and J. V. Hajnal, "Fast quantitative MRI using controlled saturation magnetization transfer," *Magn. Reson. Med.*, vol. 81, no. 2, pp. 907–920, Feb. 2019.